DESY 94-033
March 1994

ISSN 0418-9833

Energy Flow and Charged Particle Spectra in Deep Inelastic Scattering at HERA

H1 Collaboration

Abstract

Global properties of the hadronic final state in deep inelastic scattering events at HERA are investigated. The data are corrected for detector effects and are compared directly with QCD phenomenology. Energy flows in both the laboratory frame and the hadronic centre of mass system and energy-energy correlations in the laboratory frame are presented. Comparing various QCD models, the colour dipole model provides the only satisfactory description of the data. In the hadronic centre of mass system the momentum components of charged particles longitudinal and transverse to the virtual boson direction are measured and compared with lower energy lepton-nucleon scattering data as well as with e^+e^- data from LEP.

submitted to Zeitschrift für Physik C

H1 Collaboration

I. Abt[7], T. Ahmed[3], V. Andreev[24], S. Aid[13], B. Andrieu[27], R.-D. Appuhn[11], M. Arpagaus[34], A. Babaev[25], H. Bärwolff[33], J. Bán[17], P. Baranov[24], E. Barrelet[28], W. Bartel[11], U. Bassler[28], H.P. Beck[35], H.-J. Behrend[11], A. Belousov[24], Ch. Berger[1], H. Bergstein[1], G. Bernardi[28], R. Bernet[34], G. Bertrand-Coremans[4], M. Besançon[9], P. Biddulph[22], E. Binder[11], J.C. Bizot[26], V. Blobel[13], K. Borras[8], P.C. Bosetti[2], V. Boudry[27], C. Bourdarios[26], A. Braemer[14], F. Brasse[11], U. Braun[2], W. Braunschweig[1], V. Brisson[26], D. Bruncko[17], L. Büngener[13], J. Bürger[11], F.W. Büsser[13], A. Buniatian[11,37], S. Burke[19], G. Buschhorn[25], A.J. Campbell[1], T. Carli[25], F. Charles[28], D. Clarke[5], A.B. Clegg[18], M. Colombo[8], J.A. Coughlan[5], A. Courau[26], Ch. Coutures[9], G. Cozzika[9], L. Criegee[11], J. Cvach[29], S. Dagoret[28], J.B. Dainton[19], M. Danilov[23], A.W.E. Dann[22], W.D. Dau[16], M. David[9], E. Deffur[11], B. Delcourt[26], L. Del Buono[28], M. Devel[26], A. De Roeck[11], P. Di Nezza[31], P. Dingus[27], C. Dollfus[35], J.D. Dowell[3], H.B. Dreis[2], A. Drescher[8], J. Duboc[28], D. Düllmann[13], O. Dünger[13], H. Duhm[12], R. Ebbinghaus[8], M. Eberle[12], J. Ebert[32], T.R. Ebert[19], G. Eckerlin[11], V. Efremenko[23], S. Egli[35], H. Ehrlichmann[33], S. Eichenberger[35], R. Eichler[34], F. Eisele[14], E. Eisenhandler[20], N.N. Ellis[3], R.J. Ellison[22], E. Elsen[11], M. Erdmann[14], E. Evrard[4], L. Favart[4], A. Fedotov[23], D. Feeken[13], R. Felst[11], J. Feltesse[9], I.F. Fensome[3], J. Ferencei[11], F. Ferrarotto[31], K. Flamm[11], W. Flauger[11,†], M. Fleischer[11], M. Flieser[25], G. Flügge[2], A. Fomenko[24], B. Fominykh[23], M. Forbush[7], J. Formánek[30], J.M. Foster[22], G. Franke[11], E. Fretwurst[12], P. Fuhrmann[1], E. Gabathuler[19], K. Gamerdinger[25], J. Garvey[3], J. Gayler[11], M. Gebauer[8], A. Gellrich[13], M. Gennis[11], H. Genzel[1], R. Gerhards[11], L. Godfrey[7], U. Goerlach[11], L. Goerlich[6], N. Gogitidze[24], M. Goldberg[28], D. Goldner[8], A.M. Goodall[19], I. Gorelov[23], P. Goritchev[23], C. Grab[34], H. Grässler[2], R. Grässler[2], T. Greenshaw[19], H. Greif[25], G. Grindhammer[25], A. Gruber[25], C. Gruber[16], J. Haack[33], D. Haidt[11], L. Hajduk[6], O. Hamon[28], M. Hampel[1], E.M. Hanlon[18], M. Hapke[11], J. Harjes[11], R. Haydar[26], W.J. Haynes[5], J. Heatherington[20], V. Hedberg[21], G. Heinzelmann[13], R.C.W. Henderson[18], H. Henschel[33], R. Herma[1], I. Herynek[29], W. Hildesheim[11], P. Hill[5], C.D. Hilton[22], J. Hladký[29], K.C. Hoeger[22], M. Höppner[8], Ph. Huet[4], H. Hufnagel[14], N. Huot[28], M. Ibbotson[22], H. Itterbeck[1], M.-A. Jabiol[9], A. Jacholkowska[26], C. Jacobsson[21], M. Jaffre[26], T. Jansen[11], L. Jönsson[21], K. Johannsen[13], D.P. Johnson[4], L. Johnson[18], H. Jung[11], P.I.P. Kalmus[20], D. Kant[20], S. Kazarian[11], R. Kaschowitz[2], P. Kasselmann[12], U. Kathage[16], H.H.Kaufmann[33], I.R. Kenyon[3], S. Kermiche[26], C. Keuker[1], C. Kiesling[25], M. Klein[33], C. Kleinwort[13], G. Knies[11], W. Ko[7], T. Köhler[1], H. Kolanoski[8], F. Kole[7], S.D. Kolya[22], V. Korbel[11], M. Korn[8], P. Kostka[33], S.K. Kotelnikov[24], M.W. Krasny[6,28], H. Krehbiel[11], D. Krücker[2], U. Krüger[11], J.P. Kubenka[25], H. Küster[2], M. Kuhlen[25], T. Kurča[17], J. Kurzhöfer[8], B. Kuznik[32], D. Lacour[28], F. Lamarche[27], R. Lander[7], M.P.J. Landon[20], W. Lange[33], R. Langkau[12], P. Lanius[25], J.F. Laporte[9], A. Lebedev[24], A. Leuschner[11], C. Leverenz[11], S. Levonian[11,24], D. Lewin[11], Ch. Ley[2], A. Lindner[8], G. Lindström[12], F. Linsel[11], J. Lipinski[13], P. Loch[11], H. Lohmander[21], G.C. Lopez[20], D. Lüers[25,†], D. Lüke[8,11], N. Magnussen[32], E. Malinovski[24], S. Mani[7], P. Marage[4], J. Marks[10], R. Marshall[22], J. Martens[32], R. Martin[19], H.-U. Martyn[1], J. Martyniak[6], S. Masson[2], A. Mavroidis[20], S.J. Maxfield[19], S.J. McMahon[19], A. Mehta[22], K. Meier[15], D. Mercer[22], T. Merz[11],

C.A. Meyer[35], H. Meyer[32], J. Meyer[11], S. Mikocki[6,26], E. Monnier[28], F. Moreau[27], J. Moreels[4], J.V. Morris[5], K. Müller[35], P. Murín[17], S.A. Murray[22], V. Nagovizin[23], B. Naroska[13], Th. Naumann[33], G. Nawrath[8], P.R. Newman[3], D. Newton[18], D. Neyret[28], H.K. Nguyen[28], F. Niebergall[13], C. Niebuhr[11], R. Nisius[1], G. Nowak[6], G.W. Noyes[3], M. Nyberg[21], H. Oberlack[25], U. Obrock[8], J.E. Olsson[11], S. Orenstein[27], F. Ould-Saada[13], C. Pascaud[26], G.D. Patel[19], E. Peppel[11], S. Peters[25], H.T. Phillips[3], J.P. Phillips[22], Ch. Pichler[12], W. Pilgram[2], D. Pitzl[34], S. Prell[11], R. Prosi[11], G. Rädel[11], F. Raupach[1], K. Rauschnabel[8], P. Reimer[29], S. Reinshagen[11], P. Ribarics[25], V. Riech[12], J. Riedlberger[34], S. Riess[13], M. Rietz[2], S.M. Robertson[3], P. Robmann[35], R. Roosen[4], K. Rosenbauer[1] A. Rostovtsev[23], C. Royon[9], M. Rudowicz[25], M. Ruffer[12], S. Rusakov[24], K. Rybicki[6], N. Sahlmann[2], E. Sanchez[25], D.P.C. Sankey[5], M. Savitsky[11], P. Schacht[25], P. Schleper[14], W. von Schlippe[20], C. Schmidt[11], D. Schmidt[32], W. Schmitz[2], A. Schöning[11], V. Schröder[11], E. Schuhmann[25], M. Schulz[11], B. Schwab[14], A. Schwind[33], W. Scobel[12], U. Seehausen[13], R. Sell[11], A. Semenov[23], V. Shekelyan[23], I. Sheviakov[24], H. Shooshtari[25], L.N. Shtarkov[24], G. Siegmon[16], U. Siewert[16], Y. Sirois[27], I.O. Skillicorn[10], P. Smirnov[24], J.R. Smith[7], Y. Soloviev[24], H. Spitzer[13], M. Steenbock[13], P. Steffen[11], R. Steinberg[2], B. Stella[31], K. Stephens[22], J. Stier[11], U. Stösslein[33], J. Strachota[29], U. Straumann[35], W. Struczinski[2], J.P. Sutton[3], R.E. Taylor[36,26], V. Tchernyshov[23], C. Thiebaux[27], G. Thompson[20], I. Tichomirov[23], P. Truöl[35], J. Turnau[6], J. Tutas[14], L. Urban[25], A. Usik[24], S. Valkar[30], A. Valkarova[30], C. Vallée[28], P. Van Esch[4], A. Vartapetian[11,37], Y. Vazdik[24], M. Vecko[29], P. Verrecchia[9], R. Vick[13], G. Villet[9], E. Vogel[1], K. Wacker[8], I.W. Walker[18], A. Walther[8], G. Weber[13], D. Wegener[8], A. Wegner[11], H. P.Wellisch[25], L.R. West[3], S. Willard[7], M. Winde[33], G.-G. Winter[11], Th. Wolff[34], L.A. Womersley[19], A.E. Wright[22], N. Wulff[11], T.P. Yiou[28], J. Žáček[30], C. Zeitnitz[12], H. Ziaeepour[26], M. Zimmer[11], W. Zimmermann[11] and F. Zomer[26]

[1] *I. Physikalisches Institut der RWTH, Aachen, Germany*[a]
[2] *III. Physikalisches Institut der RWTH, Aachen, Germany*[a]
[3] *School of Physics and Space Research, University of Birmingham, Birmingham, UK*[b]
[4] *Inter-University Institute for High Energies ULB-VUB, Brussels, Belgium*[c]
[5] *Rutherford Appleton Laboratory, Chilton, Didcot, UK*[b]
[6] *Institute for Nuclear Physics, Cracow, Poland*[d]
[7] *Physics Department and IIRPA, University of California, Davis, California, USA*[e]
[8] *Institut für Physik, Universität Dortmund, Dortmund, Germany*[a]
[9] *DAPNIA, Centre d'Etudes de Saclay, Gif-sur-Yvette, France*
[10] *Department of Physics and Astronomy, University of Glasgow, Glasgow, UK*[b]
[11] *DESY, Hamburg, Germany*[a]
[12] *I. Institut für Experimentalphysik, Universität Hamburg, Hamburg, Germany*[a]
[13] *II. Institut für Experimentalphysik, Universität Hamburg, Hamburg, Germany*[a]
[14] *Physikalisches Institut, Universität Heidelberg, Heidelberg, Germany*[a]
[15] *Institut für Hochenergiephysik, Universität Heidelberg, Heidelberg, Germany*[a]
[16] *Institut für Reine und Angewandte Kernphysik, Universität Kiel, Kiel, Germany*[a]
[17] *Institute of Experimental Physics, Slovak Academy of Sciences, Košice, Slovak Republik*
[18] *School of Physics and Materials, University of Lancaster, Lancaster, UK*[b]

[19] *Department of Physics, University of Liverpool, Liverpool, UK*[b]
[20] *Queen Mary and Westfield College, London, UK*[b]
[21] *Physics Department, University of Lund, Lund, Sweden*[f]
[22] *Physics Department, University of Manchester, Manchester, UK*[b]
[23] *Institute for Theoretical and Experimental Physics, Moscow, Russia*
[24] *Lebedev Physical Institute, Moscow, Russia*
[25] *Max-Planck-Institut für Physik, München, Germany*[a]
[26] *LAL, Université de Paris-Sud, IN2P3-CNRS, Orsay, France*
[27] *LPNHE, Ecole Polytechnique, IN2P3-CNRS, Palaiseau, France*
[28] *LPNHE, Universités Paris VI and VII, IN2P3-CNRS, Paris, France*
[29] *Institute of Physics, Czech Academy of Sciences, Praha, Czech Republik*
[30] *Nuclear Center, Charles University, Praha, Czech Republik*
[31] *INFN Roma and Dipartimento di Fisica, Universita "La Sapienza", Roma, Italy*
[32] *Fachbereich Physik, Bergische Universität Gesamthochschule Wuppertal, Wuppertal, Germany*[a]
[33] *DESY, Institut für Hochenergiephysik, Zeuthen, Germany*[a]
[34] *Institut für Teilchenphysik, ETH, Zürich, Switzerland*[g]
[35] *Physik-Institut der Universität Zürich, Zürich, Switzerland*[g]
[36] *Stanford Linear Accelerator Center, Stanford California, USA*
[37] *Visitor from Yerevan Phys.Inst., Armenia*
[†] *Deceased*

[a] *Supported by the Bundesministerium für Forschung und Technologie, FRG under contract numbers 6AC17P, 6AC47P, 6DO57I, 6HH17P, 6HH27I, 6HD17I, 6HD27I, 6KI17P, 6MP17I, and 6WT87P*
[b] *Supported by the UK Science and Engineering Research Council*
[c] *Supported by IISN-IIKW, NATO CRG-890478*
[d] *Supported by the Polish State Committee for Scientific Research, grant No. 204209101*
[e] *Supported in part by USDOE grant DE F603 91ER40674*
[f] *Supported by the Swedish Natural Science Research Council*
[g] *Supported by the Swiss National Science Foundation*

1 Introduction

The HERA collider at DESY, which delivered the first ep interactions in 1992, has opened new kinematical domains in deep inelastic lepton-nucleon scattering (DIS) in both the small x (Bjorken scaling variable) and large Q^2 (negative 4-momentum transfer squared) regions. In this paper topological properties of hadronic final states in DIS events at small x ($x < 10^{-2}$) are presented.

In the simple quark parton model of deep inelastic scattering, a quark is scattered out of the proton by the virtual boson emitted from the scattering lepton. QCD modifies this naive picture. Gluons may be radiated before (initial state radiation) and after (final state radiation) the boson-quark vertex, and the boson may also interact with a gluon inside the proton by means of a quark line (boson-gluon fusion). Probing the proton with a boson results in the materialisation of virtual QCD fluctuations inside the proton, which become visible in the hadronic final state.

The large phase space for QCD radiation at HERA makes the hadronic final state an ideal testing ground for QCD. For $x > 10^{-2}$ DIS has been well measured and can be understood theoretically in terms of the standard QCD evolution equations [1]. Novel QCD effects [2] due to increasing parton densities may be expected in the small x region, say $x < 10^{-3}$. In the low x domain the region away from the expected current jet towards the proton remnant is of particular interest in this analysis, as it may be the region most sensitive to new effects. Expectations for the properties of hadronic final states are available in the form of Monte Carlo models, which are based on standard QCD evolution and which have been tuned to provide a satisfactory description of lower energy lepton-nucleon data and of high statistics e^+e^-data. In the new high energy domain of HERA the models differ widely in their predictions. Significant differences between QCD models and the data have already been observed [3, 4].

Increased statistics allow for a more detailed investigation, both in the laboratory frame and in the hadronic centre of mass system. The data presented were obtained in 1992, when electrons of $E_e = 26.7$ GeV were collided with protons of $E_p = 820$ GeV, resulting in a centre of mass energy of $\sqrt{s} = 296$ GeV. They correspond to an integrated luminosity of 22.5 nb^{-1}. The kinematical region investigated is $10^{-4} < x < 10^{-2}$, $10 < Q^2 < 100$ GeV^2 and W about 50-200 GeV, where W is the invariant mass of the hadronic system. The data are corrected for detector effects in order to be used as an experimental reference for theoretical developments. Transverse energy flows, transverse energy-energy correlations and charged particle spectra are studied.

2 Detector Description

A detailed description of the H1 apparatus can be found elsewhere [5]. The following briefly describes the components of the detector relevant to this analysis, which makes use of the calorimeters and the central and backward tracking systems.

The hadronic energy flow and the scattered electrons are measured with a liquid argon (LAr) calorimeter and a backward electromagnetic lead-scintillator calorimeter (BEMC). Leaking hadronic showers are measured in a surrounding tail catcher.

The LAr calorimeter [6] extends over the polar angular range $4° < \theta < 153°$ with full azimuthal coverage, where θ is defined with respect to the proton beam direction ($+z$ axis). It consists of an electromagnetic section with lead absorbers and a hadronic section with steel absorbers. Both sections are highly segmented in the transverse and the longitudinal direction with about 44000 cells in total. The total depth of both calorimeters varies between 4.5 and 8 interaction lengths. The electronic noise per channel is typically between 10 and 30 MeV (1 σ equivalent energy).

Test beam measurements of the LAr calorimeter modules show an energy resolution $\sigma_E/E \approx 0.12/\sqrt{E\,[\mathrm{GeV}]} \oplus 0.01$ for electrons and $\sigma_E/E \approx 0.50/\sqrt{E\,[\mathrm{GeV}]} \oplus 0.02$ for charged pions [5, 6, 7]. The hadronic energy measurement is performed by applying a weighting technique in order to account for the non-compensating nature of the calorimeter [8]. Both the energy scales and the resolutions have been verified in the H1 experiment. By comparing the measured track momentum of electrons and positrons with their corresponding energy deposition in the LAr calorimeter, the electromagnetic energy scale is known to a precision of 3%. The absolute scale of the hadronic energy is presently known to 6%, as determined from studies of the transverse momentum (p_T) balance in DIS events.

The BEMC (depth of 22.5 radiation lengths or 1 interaction length) covers the backward region of the detector, $151° < \theta < 177°$. A major task of the BEMC is to trigger and to measure scattered electrons in DIS processes with Q^2 values ranging from 5 to 100 GeV^2. The absolute energy scale is determined by comparing the measured electron energy in the BEMC with that calculated from the angles of the hadronic system and the electron. The BEMC energy scale for electrons is known to an accuracy of 2%. Its resolution is given by $\sigma_E/E = 0.10/\sqrt{E\,[\mathrm{GeV}]} \oplus 0.42/E[\mathrm{GeV}] \oplus 0.03$ [9].

The calorimeters are surrounded by a superconducting solenoid providing a uniform magnetic field of 1.15 T parallel to the beam axis in the tracking region. The return yoke surrounding the coil is fully instrumented with a tail catcher consisting of streamer tubes with analog read-out to measure the leakage of hadronic showers. Its resolution is $\sigma_E/E \approx 1.0/\sqrt{E\,[\mathrm{GeV}]}$.

Charged particle tracks are measured in two concentric jet drift chamber modules (CJC), covering the polar angular range $15° < \theta < 165°$. Up to 56 space points can be measured for each track. The radial coordinates are derived from drift time measurements, and the z coordinates from charge division. The achieved resolutions are $\sigma_{p_T}/p_T \approx 0.009 \cdot p_T\,[\mathrm{GeV}] \oplus 0.015$ and $\sigma_\theta = 20$ mrad [5]. A backward proportional chamber (BPC), in front of the BEMC with an angular acceptance of $155.5° < \theta < 174.5°$ serves to identify electrons and to precisely measure their direction. Using information from the BPC, the BEMC and the reconstructed event vertex the polar angle of the scattered electron is known to better than 5 mrad.

A scintillator hodoscope situated behind the BEMC is used to veto proton-induced background events based on their early time of arrival compared with that for nominal electron-proton collisions.

3 Event Selection and Kinematics

For this analysis DIS events with $Q^2 < 100$ GeV^2 are used, in which the scattered electron is observed in the BEMC.

The events are triggered by requiring a cluster of more than 4 GeV in the BEMC and no time of flight veto from the scintillator hodoscope. This trigger is fully efficient for electrons with energies above 10 GeV. After reconstruction, DIS events are selected in the following way:

- The scattered electron, defined as the most energetic BEMC cluster, must have an energy larger than 14 GeV and must be associated with a space point in the BPC within 5 cm of the cluster centre of gravity. These cuts reduce photoproduction background [9].

- The BPC hit must lie less than 60 cm from the beam line, corresponding to an electron angle above 157° with respect to the nominal interaction point. In addition the electron angle θ_e has to be smaller than 172.5°, ensuring full containment of the electron shower in the BEMC.

- An event vertex, reconstructed from tracks in the central tracker within ± 50 cm of the nominal interaction point, is required to reject beam induced background and to ensure good determination of the kinematical variables. The events have a vertex distribution centred at the nominal interaction point with a σ_z of 25 cm, which reflects the length of the proton bunch.

- There has to be at least one central track fulfilling the track selection criteria given below.

- The invariant mass squared, W^2, of the hadronic system must be greater than 3000 GeV^2, ensuring substantial hadronic energy flow in the detector.

- The calorimetric energy E_F in the forward region ($3.5° < \theta < 15°$) has to be larger than 0.5 GeV.

In Fig. 1, the distribution of E_F before the cut is shown. Two distinct classes of events are observed: the bulk of the events has considerable energy in the forward region, while about 7% of the events have only very little forward energy. Events with such large rapidity gaps in the forward region have been reported by the ZEUS and H1 collaboration [10, 11]. These events are presumed to stem from diffractive-like processes which are not included in the standard QCD models used in this analysis[1], and so are removed from the sample.

The final sample contains 885 DIS events with an average Q^2 of 25 GeV^2 and with $10^{-4} < x < 10^{-2}$. The remaining beam induced background is estimated from non-colliding pilot bunch data ($< 1\%$), and the photoproduction background in the sample is estimated using Monte Carlo simulation to be less than 4 events.

[1]Only the HERWIG model (see ch. 4) generates some fraction of events with small E_F, though it does not explicitly contain diffractive processes.

The hadronic energy flow is measured using energy depositions in the calorimeter cells, with dead material corrected for. The polar angle acceptance is between 4.4° and 174°. Electronic noise in the different calorimeters is suppressed by appropriate cuts and is also included in the detector simulation by superimposing recorded events with random triggers. A full account of energy measurements in H1 can be found in [5]. It has been verified that the analysis results do not depend on details of the reconstruction method.

For the charged particle analysis CJC tracks are used which meet the following criteria:

- The track has to have a polar angle between 22° and 158°.
- The transverse momentum of the track has to lie in the range from 0.15 GeV to 10 GeV. The upper cut removes badly measured tracks.
- The track has to start in the innermost part of the jet chamber. The radial distance between the first and last measured point on the track has to exceed 10 cm.
- The track has to be constrained to the event vertex with a distance of closest approach in the x-y plane of less than 3 cm and a distance in z of less than 20 cm.

The reconstruction efficiency for tracks fulfilling the above requirements in the DIS sample is estimated from a visual scan to be $92 \pm 3\%$. Losses are due to occasional malfunctioning of readout electronics. Chamber inefficiencies affecting about 15% of the azimuthal range are taken into account in the simulation.

The event kinematics are determined using information from both the scattered electron and the hadronic system. Q^2 is calculated from the measured electron energy E'_e and polar angle θ_e,

$$Q^2 = 4\, E_e\, E'_e \cos^2 \frac{\theta_e}{2}. \tag{1}$$

The scaling variable y is determined from the hadronic final state according to

$$y = \sum_{hadrons} \frac{E_h - p_{z,h}}{2E_e}\,, \tag{2}$$

with E_h and $p_{z,h}$ being the hadron energy and its longitudinal momentum, respectively [9]. To perform the sum over all hadrons a combination of calorimetric measurements and reconstructed charged tracks in the central region is used [9]. The measurement of y is made using the hadronic final state in preference to the electron. This has two advantages: the precision is greater for small y and the influence of QED radiation from the lepton lines on the measured kinematics is reduced. The scaling variable x is then derived via $x = Q^2/(ys)$, and $W^2 = m_p^2 + sy - Q^2$.

The transformation to the hadronic centre of mass system (CMS), defined by the rest system of the proton and the exchanged boson, is determined by the above kinematic variables. The orientation of the CMS is such that the direction of the exchanged boson defines the positive z^* axis.

4 QCD Models

The data are compared to a number of QCD inspired models in the form of Monte Carlo generators. They employ different ways of generating QCD emissions: first order QCD matrix elements, or parton showers to all orders in the leading logarithmic approximation (modelled either as bremsstrahlung like cascades or as emissions from colour dipoles), or a combination of the two. A more detailed description of the models can be found in the appendix and in [12]. For illustration, the naive quark parton model (QPM) without any gluon radiation, is also compared to the data, in which hadrons are produced from fragmentation of the string between the current quark and the remnant di-quark.

The model denoted here as MEPS [13] incorporates the QCD matrix elements to first order, with additional soft emissions generated by adding leading log parton showers.

Two different pure parton shower models are compared to the data, referred to as PSWQ [13] and HERWIG [14]. Both are based on leading log parton showers, but they differ in their way of emulating QCD coherence effects.

In the colour dipole model [15], gluons are emitted from a chain of independently radiating dipoles which are spanned by colour connected partons. Since all radiation is assumed to stem from the dipole formed by the struck quark and the remnant, boson-gluon fusion events cannot be generated in this way, they are instead taken from the QCD matrix elements.

The CDM, MEPS and PSWQ models use the Lund string fragmentation model [16] for the hadronisation of the generated partons, while HERWIG makes use of a cluster fragmentation model [17]. In addition, HERWIG uses a soft underlying event, known from minimum-bias $p\bar{p}$ collsions to model the remnant fragmentation. The MRS $D^{-'}$(DIS) structure function parametrisation [18], which is close to the recent F_2 structure function results obtained at HERA [9, 19], is used for the Monte Carlo generation.

5 Results

In the quark parton model the hadronic final state consists of a current quark, scattered at large angles into the detector, and a remnant di-quark almost parallel to the incident proton. The transverse momentum of the scattered electron is essentially balanced by the current quark (and to a lesser extent by the target remnant). With QCD, radiated soft and hard gluons populate the region between the struck quark and the di-quark. Hard parton emission in QCD Compton and boson-gluon fusion processes leads to two well separated partons, in addition to the target remnant. Non-perturbative hadronisation and particle decays tend to wash out the underlying parton topology. However, perturbative QCD effects should still be observable, particularly in the region between the current quark and the diquark.

In the following, QCD effects in DIS events are studied in terms of the flow of transverse energy in the hadronic final state, energy-energy correlations and in terms of charged particle spectra. Since the event topology strongly depends on the kinematic variables x and Q^2, energy flows and correlations are presented separately for events with $x > 10^{-3}$ (2/3 of the sample) and $x < 10^{-3}$. The latter region is of particular interest as it has not

yet been explored much experimentally.

The data are corrected for detector effects by dividing bin-by-bin with appropriate correction factors. Bin widths are chosen not smaller than the experimental resolutions obtained from Monte Carlo studies. An extensive discussion of this method can be found for example in [20]. The correction functions are determined from Monte Carlo simulations of the H1 detector response. The results of the event generation are fed into the H1 detector simulation program containing a detailed description of the H1 detector geometry and which is based on the GEANT package [21].

Monte Carlo events are processed through the same reconstruction and analysis chain as the data. The calorimetric response in the simulation program has been tuned to test-beam results [22]. Cosmic tracks and reconstructed K^0_S in the data have been used to check the simulation of the tracking detector.

The correction factors for each bin are defined as the ratios between the reconstructed and the generated values in the Monte Carlo simulation. Generated quantities are determined at the level of generated particles for events satisfying the physics selection criteria, i.e. $E'_e > 14$ GeV, $157° < \theta_e < 172.5°$, $W^2 > 3000$ GeV^2, and $E_F(3.5° < \theta < 15°) > 0.5$ GeV. Particles for the energy flow analysis have to be within the calorimeter region where a fully contained measurement is possible ($4.4° < \theta < 174°$), and for the charged particle analysis they have to be in the $+z^*$ hemisphere of the hadronic CMS. Corrections for particles outside these acceptances are not applied. The reconstructed quantities are obtained after full detector simulation and reconstruction in the same way as for real data. In using this procedure the presented results become detector independent and are valid for DIS events satisfying the physics selection cuts. The CDM generator (with the MRS D$^-$ structure function [23]) has been chosen to determine the correction factors as it provides the best description of the data which is necessary for the bin-by-bin correction technique to be applicable. The CDM generator provides not only a good description of the energy flows but also reproduces the distribution of the energy within the energy depositions in the calorimeter and the number of energy depositions. It has been verified in Monte Carlo studies that these bin-by-bin corrections are adequate to reproduce the true distributions also for models other than the one with which the correction functions were derived. This justifies using only one iteration to derive the corrections.

To study the influence of QED corrections the CDM has been used, where the first order QED corrections are generated by the HERACLES Monte Carlo [24]. QED radiative effects on the measured distributions are at most 5 %, but generally much smaller. They have not been corrected for and are included in the systematic error.

5.1 Energy Flows

The corrected transverse energy flow in the laboratory system is presented in Fig. 2a for $x < 10^{-3}$ as a function of pseudorapidity, $\eta = -\ln \tan \frac{\theta}{2}$. The distribution is normalized to the number of events N. A steep rise of the transverse energy flow is observed at negative values of η (i.e. the backward region), reaching a maximum of $E_T \approx 3$ GeV per unit of rapidity in the central region of the detector and then levelling off to $E_T \approx 2$ GeV per unit of rapidity in the forward region. For events with $x > 10^{-3}$, see Fig. 2b, the onset

of the transverse energy flow is in the central detector, and the maximum value of E_T is shifted towards the forward region. Such a behaviour is expected, since in the QPM the struck quark is scattered further into the forward direction of the laboratory system with increasing x.

From the kinematic variables y and Q^2 the pseudorapidity $\eta_q = -\ln\tan\frac{\theta_q}{2}$ can be calculated, where

$$\cos\theta_q = 1 - \frac{2E_e y}{E_e y + Q^2(1-y)/(4E_e y)} \; . \tag{3}$$

This direction coincides with the current quark direction in the QPM, but is not necessarily related to the directions of the jets observed in the events. In Fig. 3 the transverse energy flow is shown with respect to this 'current quark' direction, i.e. as a function of the pseudorapidity distance $\Delta\eta = \eta - \eta_q$. The maximum E_T flow around the 'current quark' direction is always shifted towards the direction of the proton remnant, the shift being larger at small x. Comparing with the QPM curve, which is strongly peaked very close to the 'current quark' direction, the shift observed in the data can be attributed to QCD radiation. For $x < 10^{-3}$ the data show a plateau of $E_T \approx 2$ GeV per unit of rapidity away from the 'current quark', the drop at $\Delta\eta \gtrsim 4$ is due to the detector acceptance. For the large x data the maximum E_T is higher. A plateau is not observed, because the event kinematics boosts the hadronic system more into the forward region and the detector acceptance has a severe effect on the measurements for $\Delta\eta \gtrsim 2.5$.

In the hadronic CMS the QPM 'current quark' direction coincides with the direction of the exchanged boson ($+z^*$). In the CMS transverse energies are not obscured by a boost to the laboratory system and allow a more direct observation of QCD radiation. Fig. 4 shows the transverse energy flow in the hadronic CMS as a function of the pseudorapidity, Table 1 lists these values. The current hemisphere, $\eta^* > 0$, exhibits a plateau which is almost flat at $E_T^* \approx 2$ GeV per unit of rapidity. The pseudorapidity distribution is slightly wider for the lower x data. The target remnant at $\eta^* < 0$ is essentially not observed due to the calorimeter acceptance of the detector. A comparison with the QPM shows that the larger part of the transverse energy is generated by QCD radiation.

Finally in Fig. 5, the mean transverse energy in the hadronic CMS is given as a function of W^2, providing an overall measure of the parton radiation activity. The mean transverse energy rises with increasing W^2, as expected from the increasing phase space for QCD radiation. A slight rise is seen for the QPM too, however, this can be attributed to the increased multiplicity which leads to a higher overall E_T^* being produced in the non-perturbative hadronisation step. The slope is reproduced by the QCD models, but they differ in their absolute prediction.

The corrections and uncertainties are discussed here for Fig. 2a as an example; similar considerations hold for the other distributions. The correction functions used to obtain these energy flows vary by 10% around 1.0 in the central barrel part of the calorimeter, rise up to factors of ≈ 1.8 in the forward region and in the backward part it drops to ≈ 0.6 (see Fig. 6). The increase in the forward region is due to secondary interactions in dead material in front of the calorimeter, and to a lesser extent due to the calorimetric shower spread of the steeply falling angular particle distribution. The losses in the backward calorimeters reflect the limited hadronic response of the detectors involved. The dependence on the shower model describing hadronic cascades in the detector has been

studied by comparing simulations with the GHEISHA [25] and FLUKA [26] packages and is found to be less than 5%. The correction functions depend only weakly on the choice of QCD model (CDM or MEPS: differences up to 5% in general) and structure function (MRS D^- or MRS D^0: differences $< 3\%$). Including the hadronic energy scale error the total systematical uncertainty is about the 10% level, and less than the statistical error of the data. Only in the BEMC region are the uncertainties larger but they are of less importance for this measurement.

Though events with visible rapidity gaps are removed, the influence of a possible contamination by diffractive events on the correction functions has been studied using the RAPGAP [27] generator. This generator produces diffractive events, some of which survive the selection criteria used for this analysis. However, from an estimation of the total cross section this surviving diffractive contribution is less than 10% of the DIS sample, and those events look similar to events generated by the MEPS generator in terms of energy flows, so the correction function is not affected.

It has been estimated from Monte Carlo studies that the remaining photoproduction background could lead to a systematic overestimation of the transverse energy flow in the laboratory system for the lower x bin of up to 5 % within a restricted pseudorapidity range $0 < \eta < 2$. This effect has been included in the sytematic error.

The investigated QCD models offer a large variety of predictions for the presented energy flow measurements. Only the CDM model is in reasonable agreement with the data, although at large x it falls somewhat below them. All other models differ significantly from the data with respect to the shape of the distributions and/or the absolute amount of transverse energy, in particular towards the remnant direction. HERWIG gives a good description of the average E_T^* produced (Fig. 5), but the E_T^*-flow as a function of pseudorapidity differs greatly from the data. The discrepancies in the target remnant direction are more pronounced at $x < 10^{-3}$. Most models predict too little energy in the remnant direction, HERWIG and CDM being the exceptions. This agrees with previously published uncorrected data [3, 4].

5.2 Energy-Energy Correlations

Energy-energy correlations (EEC) and their asymmetries are a powerful tool in e^+e^- annihilation experiments for discriminating against various QCD models and for determining the strong coupling constant α_s, since these distributions are largely independent of the hadronisation of the primary partons [28].

Similar investigations can be done in deep inelastic ep interactions when working in the hadronic CMS. At HERA, however, one is severely limited by the losses of particles belonging to the proton remnant in the beam pipe. A way out of this difficulty has been proposed [29], namely to study transverse energy flow correlations in the laboratory system. Denoting for each event the transverse energy $E_{T\,i}$, the pseudorapidity η_i and the azimuth ϕ_i of each calorimeter cell (for detector or simulated data)[2] or each particle (for Monte Carlo generator data) i in the laboratory system, a distance between two objects

[2]Technically the energies of all calorimeter cells are projected into an η-ϕ grid of width $\Delta\eta = \Delta\phi = 0.15$ in order to align them along the shower axis. The directions η_i and ϕ_i of each grid cell i are calculated from its centre of gravity.

in the η-ϕ plane is constructed by

$$\omega_{ij}^2 \;=\; (\eta_i - \eta_j)^2 + (\phi_i - \phi_j)^2 \; . \tag{4}$$

Using $p_{T\,e}^2 = Q^2\,(1-y)$ of the scattered electron as a suitable normalization, the transverse energy-energy correlation at a distance ω can be defined as

$$\Omega(\omega) \;=\; \frac{1}{N\,\Delta\omega} \sum_N \sum_{i,j;i\neq j} \frac{E_{T\,i}\,E_{T\,j}}{p_{T\,e}^2} \int_{\omega-\frac{\Delta\omega}{2}}^{\omega+\frac{\Delta\omega}{2}} \delta(\omega' - \omega_{ij})\;\mathrm{d}\omega' \; , \tag{5}$$

where autocorrelations $i = j$ are excluded, $\Delta\omega$ is the bin width and the sum is made over all N events. The effects of the beam hole become less important, since the choice of transverse energies suppresses the target remnant jet and enhances the current jet and its QCD radiation effects.

For the above EEC definition the pseudorapidity η and the azimuthal angle ϕ are not well suited for particles or energy clusters close to the beam pipe. Particles belonging to the remnant jet are spread over large η and ϕ ranges, thus diluting the collimation of the jet in the η-ϕ plane. In order to reduce the influence of the remnant jet fragmentation and the energy flow in the forward part of the detector, a cut on the polar angle of the calorimeter cells and Monte Carlo generator particles of $\theta > 8°$ is applied to the present EEC analysis.

The corrected transverse energy-energy correlations are shown in Fig. 7 and listed in Table 2. The correction function is constant and close to 1.3 (within ± 0.1) up to $\omega < 5$ for $x < 10^{-3}$. At $x > 10^{-3}$ the corrections vary between 1.2 and 1.6 for $\omega < 4$ and start to rise up to ~ 2.5 with large uncertainties at larger ω values. The model dependence of the corrections introduces a systematic error of 10–15%, but rises up to 30% for $\omega > 4$. The dependence on the structure function used for correction contributes an uncertainty of about 5%. The uncertainty of the calorimeter energy scales gives an overall systematic error of 12%. Note that the statisical errors of the EEC distributions are not independent of each other, since each energy contributes many times.

For $x < 10^{-3}$ (Fig. 7a) the data rise continuously towards a pronounced correlation around $\omega \sim \pi$ (roughly a factor of 2 stronger than at low ω), followed by a steep decrease. For $x > 10^{-3}$ (Fig. 7b) the EEC exhibit a rather flat distribution with two distinct enhancements at low ω and $\omega \sim \pi$. Correlations within a jet-like object are expected to populate the region at low ω. Furthermore the transverse energy flow shows a wide spread in azimuth in the forward region of the detector. This leads to the expectation of a rather flat EEC distribution up to an ω given essentially by the maximum azimuthal particle separation, followed by a decrease determined by the separation in pseudorapidity. Comparing the data with the QPM prediction, apart from the differrent overall scales, the data show stronger enhancements at low ω and around $\omega \sim \pi$. The excess at $\omega \sim \pi$ can be attributed to $2 + 1$ jet configurations, *e.g.* boson-gluon fusion and QCD Compton processes. In the hadronic CMS the two parton jets are produced opposite in azimuth, a feature which is approximately preserved in the laboratory system. The ω range covered is shorter at high x, which can be understood by the fact that the partons are scattered more into the forward part of the detector (see Fig. 2), thus reducing the separation in pseudorapidity between the observed particles. The mean values of $\Omega(\omega)$ are considerably smaller for the high x data, because here the electron has on average a larger $p_{T\,e}$.

None of the investigated QCD models describes the data perfectly, the discrepancies being largest at low x. The best representation of the data is provided by the MEPS model. This is somewhat surprising, since it fails to reproduce the energy flow in the forward detector region. The CDM model gives a reasonable account of the shape of the distributions, however, it always lies above the data and may be just consistent within the systematic energy scale uncertainty. The PSWQ model describes the shape of the distributions reasonably, but lies systematically above the data outside the systematic energy scale uncertainty. HERWIG provides a fair description of the data at large x, while the shape at small x is not reproduced.

5.3 Charged Particle Spectra

In the following charged particle spectra are presented in the hadronic CMS for longitudinal (p_z^*) and transverse (p_T^*) momentum components with respect to the virtual boson direction. The data are corrected over the full $+z^*$ hemisphere taking into account losses due to the limited central tracker acceptance.

The scaled longitudinal momentum is defined by $x_F = 2p_z^*/W$. The x_F spectra for the three different W ranges between 50 and 200 GeV are given in Table 3 and displayed in Fig. 8. Acceptance corrections are generally 20-30%, of which 15% are due to a well understood chamber inefficiency. However, for the lowest W range they rise to 60% at $x_F = 0.03$ due to particles leaving the tracker acceptance in the $+z$ direction. For the largest bin of W, the corrections decrease from 60% at $x_F = 0.01$ to 25% at $x_F = 0.03$, and then rise slowly again to 50 % at the largest x_F bin due to particles lost in the $-z$ direction. The systematic error due to model dependent corrections rises from about 5% in the lowest x_F bin to about 25% in the largest x_F bin. The x_F resolution due to the boost to the CMS is 13%. The uncertainty in the calorimetric scale affects the boost to the hadronic CMS and leads to errors between 3 and 15 %, rising with x_F. The determination of the track finding inefficiency introduces a small systematic error of 3%. Due to the large x_F bins, the momentum resolution does not contribute to the systematic error.

The spectra fall steeply with x_F. Within the experimental errors the distributions for the different W ranges agree with each other, in accordance with the simple scaling hypothesis. Scaling violations due to QCD radiation are presently not resolvable within the data. All models are able to describe the data within errors, and as an example CDM is shown in Fig. 8a.

In Fig. 8b the data averaged over all values of W are compared to lepton-nucleon scattering at much lower $< W >= 14$ GeV from EMC [30]. For $x_F \gtrsim 0.15$ the slope of the H1 data appears steeper than for the EMC data, an indication of scaling violation. At smaller x_F a proliferation of particles is observed when going from the EMC to HERA energies, which is correlated with the increase of phase space for the fragmentation process: starting with a larger energy of the primary quark, more particles can be produced in the fragmentation chain until there is not enough energy left for producing a pion.

Data from a different reaction, e^+e^- annihilation at LEP [31], at a similar W, can also be compared to the H1 data[3]. The DELPHI data agree well with the H1 data for

[3]Due to the large W and the dominantly small p_T^*, the H1 spectra in terms of $x_F = 2p_z^*/W$, $x_E = 2E^*/W$ and $x_p = 2p^*/W$ differ by less than the size of the symbols, and can be compared directly to the

$x_F > 0.15$. At smaller x_F, the H1 data lie significantly below the LEP data.

At HERA, contributions to the transverse momenta of particles from intrinsic p_T in the proton and from fragmentation are expected to be small, leaving gluon radiation as the dominating source. As a sensitive measure of this effect the so-called seagull plot is presented, which gives the average transverse momentum squared, p_T^{*2}, as a function of x_F. The H1 data are given in Table 4 and displayed in Fig. 9. Corrections applied vary from 2% at small x_F to 27% at large x_F. The systematic errors take into account the model dependence of the corrections (3-7%, rising with x_F), the calorimeter calibration (similar magnitude) and the dependence of the result on the choice of the $p_T < 10$ GeV cut (affecting the data up to 10% in the highest x_F bin).

With increasing x_F, the average transverse momentum squared increases by about an order of magnitude. Comparing the H1 data at $< W >= 117$ GeV to EMC data [30] at $< W >= 14$ GeV, much larger transverse momenta are observed. This increase has to be attributed to increased QCD radiation. The QPM gives a factor of about 5-10 less $< p_T^{*2} >$.

As to the strength of this effect, the models differ in their prediction. MEPS and CDM describe the data adequately, while PSWQ is only marginally compatible with the data. HERWIG differs significantly from the data, not only in magnitude, but also in the shape of the spectrum.

6 Conclusions

Observables describing some general features of the hadronic final state in deep inelastic scattering events have been measured in a new kinematic domain of low x and large W where new QCD effects can be expected. Exact QCD calculations for these observables are not available, rather there exist a number of phenomenological models, which are based on different approximations of the underlying QCD processes. These models have been used for Monte Carlo simulations of the hadronic final state, and make very different predictions. The best overall description of the H1 data is provided by the colour dipole model. All other models fail to describe the flow of transverse energy, the energy-energy-correlation, or the transverse momenta of charged particles. Straightforward variation of their parameters did not result in a significant improvement of the overall description of the data. The discrepancies are largest at small x and towards the proton remnant.

Acknowledgements. We are grateful to the HERA machine group whose outstanding efforts made this experiment possible. We appreciate the immense effort of the engineers and technicians who constructed and maintained the detector. We thank the funding agencies for financial support. We acknowledge the support of the DESY technical staff. We also wish to thank the DESY directorate for the hospitality extended to the non-DESY members of the collaboration. We thank B. Andersson, J. Chyla, T. Haas, G. Ingelman, L. Lönnblad and M. Seymour for valuable discussions.

x_p spectrum from DELPHI.

Appendix A: Generators

Version numbers and the non-default parameters of the various Monte Carlo generators are listed and their features are given in more detail. Throughout, the number of flavours has been set to 5, MRS D$^{-'}$(DIS) parton distributions are used and Λ_{QCD} has been set to 190 MeV.

- **PSWQ**
  - generator: LEPTO 6.1 [13], JETSET 7.3 [16]
  - model specifications:
    PSWQ is a parton shower (PS) model incorporating QCD emissions to all orders in the leading logarithmic approximation. The maximum value of the evolution variable, in this case the virtuality of the emitting parton, is set to WQ. QCD coherence, i.e. the depletion of soft gluons due to destructive interference, is partly implemented by imposing strong angular ordering on the final state cascade. Interference between the initial and final state cascade is neglected.
  - parameter settings:

parameter	meaning	default value	value used
LST(8)	PS or MEPS	12	2
LST(9)	PS-scale	5	3

- **MEPS**
  - generator: LEPTO 6.1 (an error in routine LMEPS was corrected after consultation with the author) [13], JETSET 7.3 [16]
  - model specifications:
    This model implements the first order QCD matrix elements (ME) for DIS with added leading log parton showers [32]. A cut-off is used to avoid regions where the ME are divergent. The amount of emission generated by the ME depends on the value of this cut-off parameter, implemented as $y_{cut} = \frac{m_{ij}^2}{W^2}$, where m_{ij} is the invariant mass of the two partons generated by the ME. The maximum of the evolution variable (again the virtuality) of the PS is essentially given by the invariant mass of the two partons. For events with no hard radiation produced at the matrix elements stage the parton shower evolution variable has a maximum given by $y_{cut}W^2$.
  - parameter settings:

    all at their default values

- **CDM**
  - generator: LEPTO 6.1 [13], ARIADNE 4.03 [15], JETSET 7.3 [16]

– model specifications:
CDM provides an implementation of the colour dipole model with the approximation of a chain of independently radiating dipoles connected via the emitted gluons. The maximum of the evolution variable (in this case the p_T^2 of the emitted gluon) for the first radiated gluon is given by $(\frac{W}{2})^{4/3}\mu^{2/3}$, as a result of the proton remnant being an extended coloured object with an inverse radius $\mu = 0.6$ GeV [33]. This leads to suppressed emissions in the target region, depending on the value of μ. Subsequent emissions are ordered in decreasing p_T^2, which ensures that the approximation of independent dipoles is valid and QCD coherence effects are taken into account. ARIADNE uses LEPTO for generating the electroweak part of the process and utilises the ME to generate boson-gluon fusion events [32]. In the case of boson-gluon fusion both the quark and the antiquark form a dipole with the remnant. Further emissions of the two dipoles can be restricted by setting the maximum allowed p_T^2 for the first emitted gluon to the average p_T^2 of the $q\bar{q}$-pair in the hadronic CMS. Theoretical considerations suggest that emissions with higher p_T's should be highly suppressed [34]. Applying this procedure without changes to the model parameters does not result in significant differences from the default in ARIADNE for the distributions discussed in this analysis, they are less than 3%.

– parameter settings:

default values according to EMC/DELPHI tuning

- **HERWIG**

– generator: HERWIG 5.7 [14]

– model specifications:
HERWIG provides a leading log parton shower model obeying QCD coherence in both the initial and final state cascade. A coherence condition derived from the colour connections of the partons of the hard subprocess fixes the maximum value of the evolution variable [35]. This takes interference between the initial and the final state into account. Only in HERWIG is an attempt made to include some of the additional QCD effects that arise at small x [14]. HERWIG uses a cluster fragmentation model employing non-perturbative splitting of gluons into colourless clusters. The model for the soft underlying event (s.u.e.) is basically a parametrisation of the existing minimum-bias data in $p\bar{p}$ with necessary modifications for the cluster fragmentation model and DIS. The fraction of events with s.u.e. can be varied between 0 and 1, where 1 is the default value used.

– parameter settings:

parameter	meaning	default value	value used
IPROC	process number	none	9000 (DIS with s.u.e.)
CLMAX	max. cluster mass [GeV]	3.5	3.0
PSPLT	cluster split spectrum	1.0	0.5
QSPAC	cut-off for initial PS	2.5	2.0
PTRMS	intrinsic k_T [GeV]	0.0	0.7

Appendix B: Tables

η^*	$x < 10^{-3}$ $1/N\,\mathrm{d}E_T^*/\mathrm{d}\eta^*$ (GeV)	$x > 10^{-3}$ $1/N\,\mathrm{d}E_T^*/\mathrm{d}\eta^*$ (GeV)
$-1.25 - -1.00$	$0.34 \pm .07 \pm .04$	
$-1.00 - -0.75$	$1.06 \pm .13 \pm .09$	$0.10 \pm .02 \pm .01$
$-0.75 - -0.50$	$1.43 \pm .13 \pm .10$	$0.40 \pm .05 \pm .03$
$-0.50 - -0.25$	$1.91 \pm .16 \pm .12$	$0.81 \pm .08 \pm .04$
$-0.25 - -0.00$	$1.76 \pm .16 \pm .10$	$1.24 \pm .09 \pm .05$
$0.00 - 0.25$	$1.89 \pm .17 \pm .11$	$1.52 \pm .10 \pm .06$
$0.25 - 0.50$	$1.90 \pm .17 \pm .10$	$1.90 \pm .13 \pm .08$
$0.50 - 0.75$	$2.07 \pm .18 \pm .10$	$1.82 \pm .12 \pm .07$
$0.75 - 1.00$	$2.00 \pm .17 \pm .10$	$1.81 \pm .11 \pm .07$
$1.00 - 1.25$	$2.19 \pm .22 \pm .11$	$1.89 \pm .13 \pm .07$
$1.25 - 1.50$	$1.95 \pm .20 \pm .09$	$2.05 \pm .13 \pm .08$
$1.50 - 1.75$	$1.95 \pm .22 \pm .10$	$2.18 \pm .16 \pm .08$
$1.75 - 2.00$	$2.10 \pm .23 \pm .11$	$2.09 \pm .16 \pm .08$
$2.00 - 2.25$	$2.51 \pm .29 \pm .13$	$2.26 \pm .17 \pm .09$
$2.25 - 2.50$	$2.01 \pm .22 \pm .10$	$2.35 \pm .17 \pm .10$
$2.50 - 2.75$	$3.00 \pm .44 \pm .15$	$2.31 \pm .16 \pm .10$
$2.75 - 3.00$	$2.00 \pm .24 \pm .10$	$2.33 \pm .18 \pm .11$
$3.00 - 3.25$	$2.41 \pm .26 \pm .12$	$2.06 \pm .16 \pm .11$
$3.25 - 3.50$	$2.14 \pm .25 \pm .11$	$1.35 \pm .12 \pm .08$
$3.50 - 3.75$	$1.75 \pm .23 \pm .09$	$0.90 \pm .09 \pm .06$
$3.75 - 4.00$	$1.36 \pm .17 \pm .08$	$0.69 \pm .08 \pm .05$
$4.00 - 4.25$	$0.85 \pm .11 \pm .05$	$0.41 \pm .05 \pm .04$
$4.25 - 4.50$	$0.55 \pm .09 \pm .04$	$0.31 \pm .04 \pm .03$
$4.50 - 4.75$	$0.50 \pm .08 \pm .04$	$0.15 \pm .02 \pm .02$
$4.75 - 5.00$	$0.27 \pm .06 \pm .03$	$0.08 \pm .02 \pm .01$
$5.00 - 5.25$	$0.17 \pm .04 \pm .03$	$0.04 \pm .01 \pm .01$
$5.25 - 5.50$	$0.10 \pm .03 \pm .02$	$0.03 \pm .01 \pm .01$

Table 1: Corrected transverse energy flow E_T^*in the hadronic centre of mass system for two different x ranges as a function of the pseudorapidity η^*. The first error is statistical, the second systematic; the overall systematic error of 6% of the energy scale is not included.

ω	$x < 10^{-3}$ $\Omega(\omega)$	$x > 10^{-3}$ $\Omega(\omega)$
0.15 – 0.30	$1.28 \pm 0.28 \pm 0.20$	$0.46 \pm 0.04 \pm 0.04$
0.30 – 0.45	$1.34 \pm 0.17 \pm 0.14$	$0.57 \pm 0.05 \pm 0.05$
0.45 – 0.60	$1.28 \pm 0.15 \pm 0.06$	$0.53 \pm 0.04 \pm 0.04$
0.60 – 0.75	$1.38 \pm 0.17 \pm 0.05$	$0.52 \pm 0.03 \pm 0.04$
0.75 – 0.90	$1.25 \pm 0.14 \pm 0.09$	$0.47 \pm 0.03 \pm 0.04$
0.90 – 1.05	$1.36 \pm 0.15 \pm 0.14$	$0.44 \pm 0.03 \pm 0.03$
1.05 – 1.20	$1.44 \pm 0.17 \pm 0.17$	$0.42 \pm 0.03 \pm 0.03$
1.20 – 1.35	$1.39 \pm 0.15 \pm 0.17$	$0.41 \pm 0.03 \pm 0.03$
1.35 – 1.50	$1.48 \pm 0.16 \pm 0.18$	$0.42 \pm 0.03 \pm 0.03$
1.50 – 1.65	$1.43 \pm 0.17 \pm 0.16$	$0.43 \pm 0.03 \pm 0.03$
1.65 – 1.80	$1.50 \pm 0.17 \pm 0.16$	$0.44 \pm 0.03 \pm 0.03$
1.80 – 1.95	$1.59 \pm 0.18 \pm 0.15$	$0.43 \pm 0.03 \pm 0.03$
1.95 – 2.10	$1.63 \pm 0.18 \pm 0.14$	$0.43 \pm 0.03 \pm 0.03$
2.10 – 2.25	$1.69 \pm 0.18 \pm 0.12$	$0.43 \pm 0.03 \pm 0.03$
2.25 – 2.40	$1.84 \pm 0.20 \pm 0.12$	$0.45 \pm 0.03 \pm 0.03$
2.40 – 2.55	$1.90 \pm 0.20 \pm 0.10$	$0.45 \pm 0.03 \pm 0.03$
2.55 – 2.70	$2.02 \pm 0.22 \pm 0.07$	$0.48 \pm 0.04 \pm 0.03$
2.70 – 2.85	$2.28 \pm 0.27 \pm 0.05$	$0.53 \pm 0.04 \pm 0.04$
2.85 – 3.00	$2.57 \pm 0.31 \pm 0.02$	$0.54 \pm 0.04 \pm 0.04$
3.00 – 3.15	$2.66 \pm 0.33 \pm 0.07$	$0.52 \pm 0.04 \pm 0.03$
3.15 – 3.30	$2.17 \pm 0.31 \pm 0.11$	$0.37 \pm 0.03 \pm 0.02$
3.30 – 3.45	$1.71 \pm 0.25 \pm 0.14$	$0.25 \pm 0.02 \pm 0.01$
3.45 – 3.60	$1.47 \pm 0.18 \pm 0.18$	$0.19 \pm 0.02 \pm 0.01$
3.60 – 3.75	$1.14 \pm 0.13 \pm 0.18$	$0.13 \pm 0.01 \pm 0.01$
3.75 – 3.90	$1.02 \pm 0.13 \pm 0.21$	$0.08 \pm 0.01 \pm 0.01$
3.90 – 4.05	$0.82 \pm 0.10 \pm 0.21$	$0.06 \pm 0.01 \pm 0.01$
4.05 – 4.20	$0.68 \pm 0.08 \pm 0.21$	$0.04 \pm 0.00 \pm 0.01$
4.20 – 4.35	$0.58 \pm 0.07 \pm 0.18$	$0.03 \pm 0.00 \pm 0.01$
4.35 – 4.50	$0.51 \pm 0.07 \pm 0.16$	
4.50 – 4.65	$0.37 \pm 0.06 \pm 0.12$	
4.65 – 4.80	$0.28 \pm 0.04 \pm 0.10$	
4.80 – 4.95	$0.27 \pm 0.05 \pm 0.09$	
4.95 – 5.10	$0.16 \pm 0.03 \pm 0.05$	
5.10 – 5.25	$0.13 \pm 0.03 \pm 0.04$	
5.25 – 5.40	$0.07 \pm 0.01 \pm 0.02$	
5.40 – 5.55	$0.03 \pm 0.01 \pm 0.01$	

Table 2: Corrected transverse energy-energy correlations $\Omega(\omega)$ for two different x ranges. The first error is statistical, the second systematic; the overall systematic error of 12% from the energy scale is not included.

	$1/N\,\mathrm{d}n/\mathrm{d}x_F$			
	W = 50-100 GeV	W = 100-150 GeV	W = 150-200 GeV	
x_F	$< W >$= 77 GeV	$< W >$ 122 GeV	$< W >$= 169 GeV	$< W >$= 117 GeV
0.00-0.02			$250 \pm 12 \pm 18$	
0.02-0.04	$67 \pm 5 \pm 5$	$69 \pm 4 \pm 3$	$59 \pm 5 \pm 5$	$64 \pm 2 \pm 5$
0.04-0.06	$36 \pm 3 \pm 3$	$37 \pm 3 \pm 2$	$42 \pm 4 \pm 5$	$38 \pm 2 \pm 3$
0.06-0.08	$24 \pm 2 \pm 2$	$21 \pm 2 \pm 2$	$29 \pm 3 \pm 4$	$24 \pm 1 \pm 2$
0.08-0.12	$18.3 \pm 1.4 \pm 1.8$	$14.8 \pm 1.2 \pm 1.3$	$15 \pm 2 \pm 2$	$16.0 \pm 0.8 \pm 1.8$
0.12-0.16	$9.0 \pm 0.9 \pm 1.2$	$11.0 \pm 1.1 \pm 1.1$	$8.8 \pm 1.3 \pm 1.1$	$9.6 \pm 0.6 \pm 1.2$
0.16-0.20	$5.9 \pm 0.8 \pm 0.8$	$5.9 \pm 0.8 \pm 0.7$	$5.8 \pm 1.1 \pm 0.8$	$6.0 \pm 0.5 \pm 0.8$
0.20-0.24	$3.8 \pm 0.6 \pm 0.5$	$5.0 \pm 0.7 \pm 0.6$	$4.7 \pm 0.9 \pm 0.7$	$4.4 \pm 0.4 \pm 0.6$
0.24-0.28	$2.1 \pm 0.4 \pm 0.3$	$2.4 \pm 0.5 \pm 0.3$	$4.2 \pm 1.0 \pm 0.6$	$2.6 \pm 0.3 \pm 0.4$
0.28-0.36	$2.5 \pm 0.4 \pm 0.4$	$1.5 \pm 0.3 \pm 0.2$	$1.8 \pm 0.4 \pm 0.4$	$1.9 \pm 0.2 \pm 0.3$
0.36-0.44	$1.3 \pm 0.3 \pm 0.3$	$0.62 \pm 0.18 \pm 0.09$	$1.2 \pm 0.4 \pm 0.3$	$0.97 \pm 0.15 \pm 0.20$
0.44-0.52	$0.6 \pm 0.2 \pm 0.2$	$0.33 \pm 0.12 \pm 0.07$	$0.4 \pm 0.2 \pm 0.1$	$0.45 \pm 0.10 \pm 0.10$

Table 3: Corrected charged particle spectra ($x_F = 2p_z^*/W$) in the hadronic CMS for three different W ranges. The first error is statistical, the second systematic.

x_F	$< p_T^{*2} >$ (GeV^2)
0.00-0.03	$0.21 \pm 0.01 \pm 0.01$
0.03-0.07	$0.39 \pm 0.03 \pm 0.03$
0.07-0.11	$0.57 \pm 0.07 \pm 0.05$
0.11-0.15	$0.72 \pm 0.17 \pm 0.06$
0.15-0.20	$0.88 \pm 0.13 \pm 0.10$
0.20-0.28	$1.20 \pm 0.28 \pm 0.17$
0.28-0.40	$1.38 \pm 0.28 \pm 0.21$
0.40-0.54	$2.40 \pm 0.72 \pm 0.65$

Table 4: Corrected values of $< p_T^{*2} >$ for charged particles in the hadronic centre of mass system as a function of x_F. The first error is statistical, the second systematic.

References

[1] V.N. Gribov and L.N. Lipatov, Sov. J. Nucl. Phys. 15 (1972) 438 and 675; G. Altarelli and G. Parisi, Nucl. Phys. 126 (1977) 297.

[2] E.A. Kuraev, L.N. Lipatov and V.S. Fadin, Sov. Phys. JETP 45 (1972) 199; Y.Y. Balitsky and L.N. Lipatov, Sov. J. Nucl. Phys. 28 (1978) 282.

[3] H1 Collab., T. Ahmed et al., Phys. Lett. B298 (1993) 469.

[4] ZEUS Collab., M. Derrick et al., Z. Phys. C59 (1993), 231.

[5] H1 Collab., I. Abt et al., "The H1 detector at HERA", DESY preprint 93-103 (1993), to be submitted to Nucl. Instr. and Meth..

[6] H1 Calorimeter Group, B. Andrieu et al., Nucl. Instr. and Meth. A336 (1993) 460.

[7] H1 Calorimeter Group, B. Andrieu et al., Nucl. Instr. and Meth. A336 (1993) 499.

[8] H.P. Wellisch et al., "Hadronic Calibration of the H1 LAr Calorimeter using Software Weighting Techniques", MPI-PhE/94-03, January 1994.

[9] H1 Collab., I. Abt et al., Nucl. Phys. B407 (1993) 515.

[10] ZEUS Collab., M. Derrick et al., Phys. Lett. B315 (1993) 481.

[11] W. Bartel, "$\sigma_{\gamma p}^{tot}$ and Diffractive Processes in Photoproduction and DIS.", to appear in Proc. of the Europhysics Conference, Marseilles, France, July 1993.
J. B. Dainton, "Results from the H1 Experiment at HERA.", in Proc. XVI International Symposium on Lepton Photon Interactions, Cornell, Ithaca, USA, August 1993, Ed. P. Drell and D. Rubin. Rutherford preprint RAL 94-12 (1994).
A. De Roeck, "Deep Inelastic Scattering at Low x, Results from the H1 Experiment.", to appear in Proc. of the Europhysics Conference, Marseilles, France, July 1993. DESY preprint 94-005 (1994).

[12] Proc. HERA workshop, Eds. W. Buchmüller and G. Ingelman, Hamburg (1991) Vol. 3.

[13] G. Ingelman, *in* Proc. HERA workshop, Eds. W. Buchmüller and G. Ingelman, Hamburg (1991) Vol. 3, 1366.

[14] G. Marchesini, B.R. Webber, G. Abbiendi, I.G. Knowles, M.H. Seymour and L. Stanco, Computer Phys. Comm. 67 (1992) 465.

[15] L. Lönnblad, Computer Phys. Comm. 71 (1992) 15.

[16] T. Sjöstrand, Computer Phys. Comm. 39 (1986) 347;
T. Sjöstrand and M. Bengtsson, Computer Phys. Comm. 43 (1987) 367, and for JETSET 7.3, T. Sjöstrand, CERN-TH-6488-92 (1992).

[17] B.R. Webber, Nucl. Phys. B238 (1984) 492.

[18] A.D. Martin, W.J. Stirling, R.G. Roberts, Phys. Lett. 306B (1993) 145, ibid. 309B (1993) 492.

[19] ZEUS Collab., M. Derrick et al., Phys. Lett. B316 (1993) 412.

[20] OPAL Collab., M.Z. Akrawy et al., Z. Phys. C47 (1990) 505.

[21] R. Brun et al., GEANT3 User's Guide, CERN–DD/EE 84–1, Geneva (1987)

[22] M. Kuhlen, *in* Proc. of the XXVI International Conference on High Energy Physics, ed. J. R. Sanford, Dallas 1992, vol. 2, p. 1787.

[23] A.D. Martin, W.J. Stirling, R.G. Roberts, Phys. Rev. D47 (1993) 867.

[24] A. Kwiatkowski, H. Spiesberger and H.-J. Möhring, Computer Phys. Comm. 69 (1992) 155.

[25] H. Fesefeldt, "The Simulation of Hadronic Showers: Physics and Applications", RWTH Aachen Pitha 85/02.

[26] P.A. Aarnio et al., CERN Fluka89 User Guide (1990).

[27] H. Jung, "Hard diffractive scattering in high-energy ep collisions and the Monte Carlo generator RAPGAP", DESY preprint 93-182 (1993), submitted to Computer Phys. Comm..

[28] L. Basham, L. Brown, S. Ellis and S. Love, Phys. Rev. Lett. 41 (1978) 1585; for recent e^+e^- analyses see OPAL Collab., P.D. Acton et al., Phys. Lett. B276 (1992) 547 and DELPHI Collab., P. Abreu et al., Z. Phys. C54 (1992) 55.

[29] M. Bengtsson, G. Ingelman and T. Sjöstrand, Nucl. Phys. B301 (1988) 554; M. Bengtsson, G. Ingelman and B. Naroska, *in* Proc. HERA Workshop, Ed. R.D. Peccei., Hamburg (1987), vol. 1, p. 281.

[30] EMC Collab., M. Arneodo et al., Z. Phys. C35 (1987) 417.

[31] DELPHI Collab., P. Abreu et al., Phys. Lett. B311 (1993) 408.

[32] N. Brook, G. Ingelman and L. Lönnblad, *in* Proc. HERA workshop, Eds. W. Buchmüller and G. Ingelman, Hamburg (1991) Vol. 1, 275.

[33] B. Andersson, G. Gustafson, L. Lönnblad and U. Pettersson, Z. Phys. C43 (1989) 625.

[34] B. Andersson, L. Lönnblad, private communication.

[35] G. Marchesini and B.R. Webber, Nucl. Phys. B310 (1988) 461.

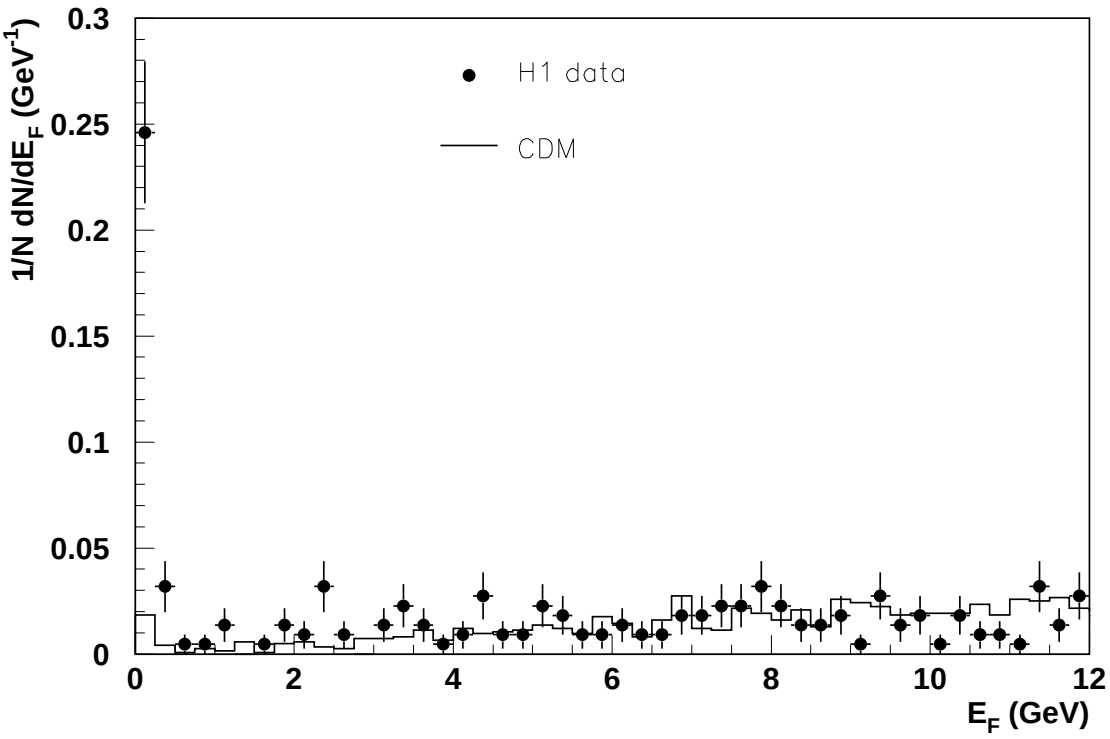

Figure 1: The energy in the forward region, $3.5° < \theta < 15°$. The data are compared with the CDM Monte Carlo (see ch. 4). Both are normalized to the number of events N.

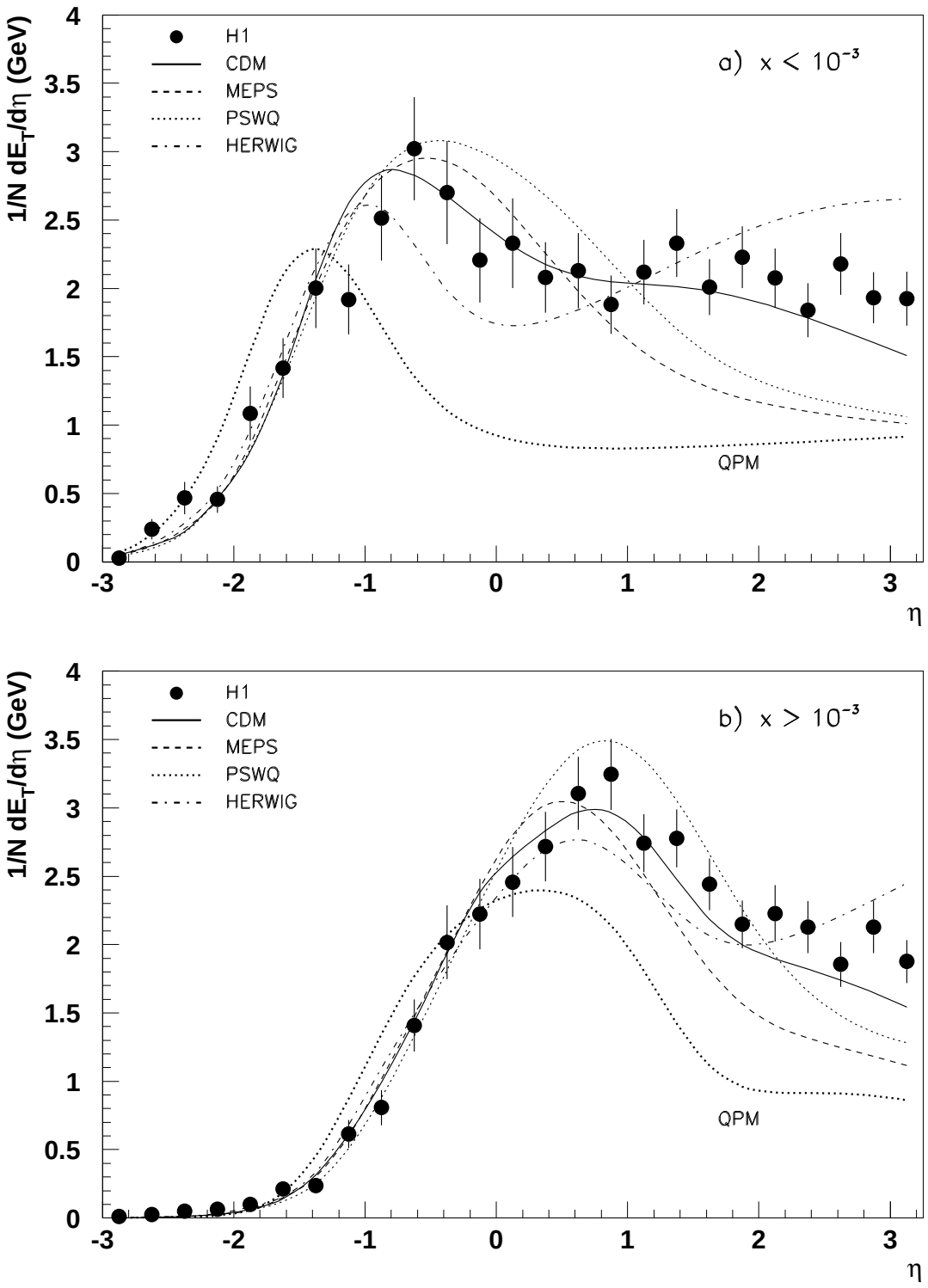

Figure 2: Transverse energy flows E_T in the laboratory system as a function of the pseudorapidity η for events with **a)** $x < 10^{-3}$ and **b)** $x > 10^{-3}$. The proton direction is to the right. The error bars contain the statistical and systematic errors added in quadrature, except for an overall 6% energy scale uncertainty.

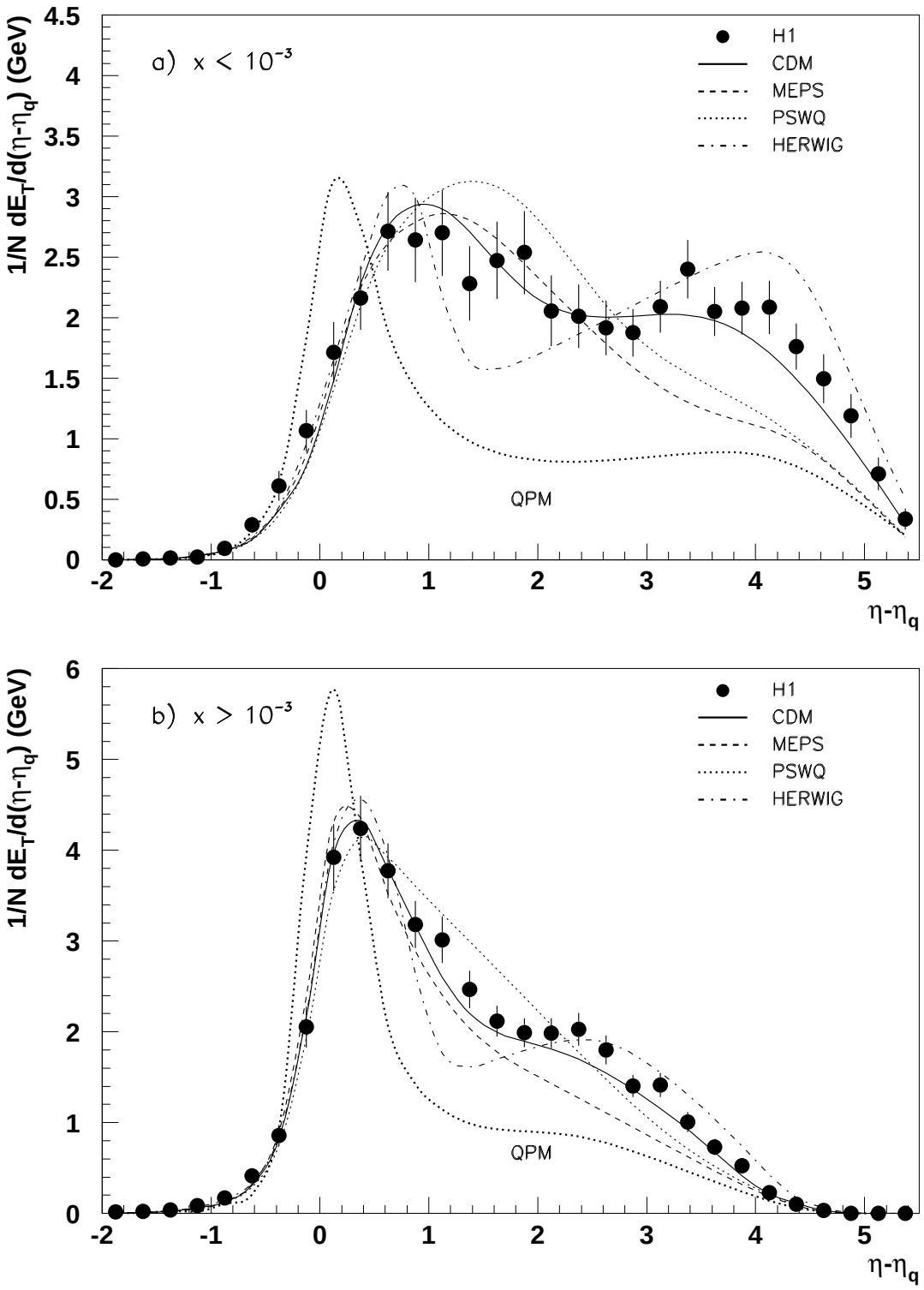

Figure 3: Transverse energy flows E_T in the laboratory system as a function of the pseudorapidity distance to the 'current quark' $\eta - \eta_q$ for events with **a)** $x < 10^{-3}$ and **b)** $x > 10^{-3}$. The proton direction is to the right. The error bars contain the statistical and systematic errors added in quadrature, except for an overall 6% energy scale uncertainty.

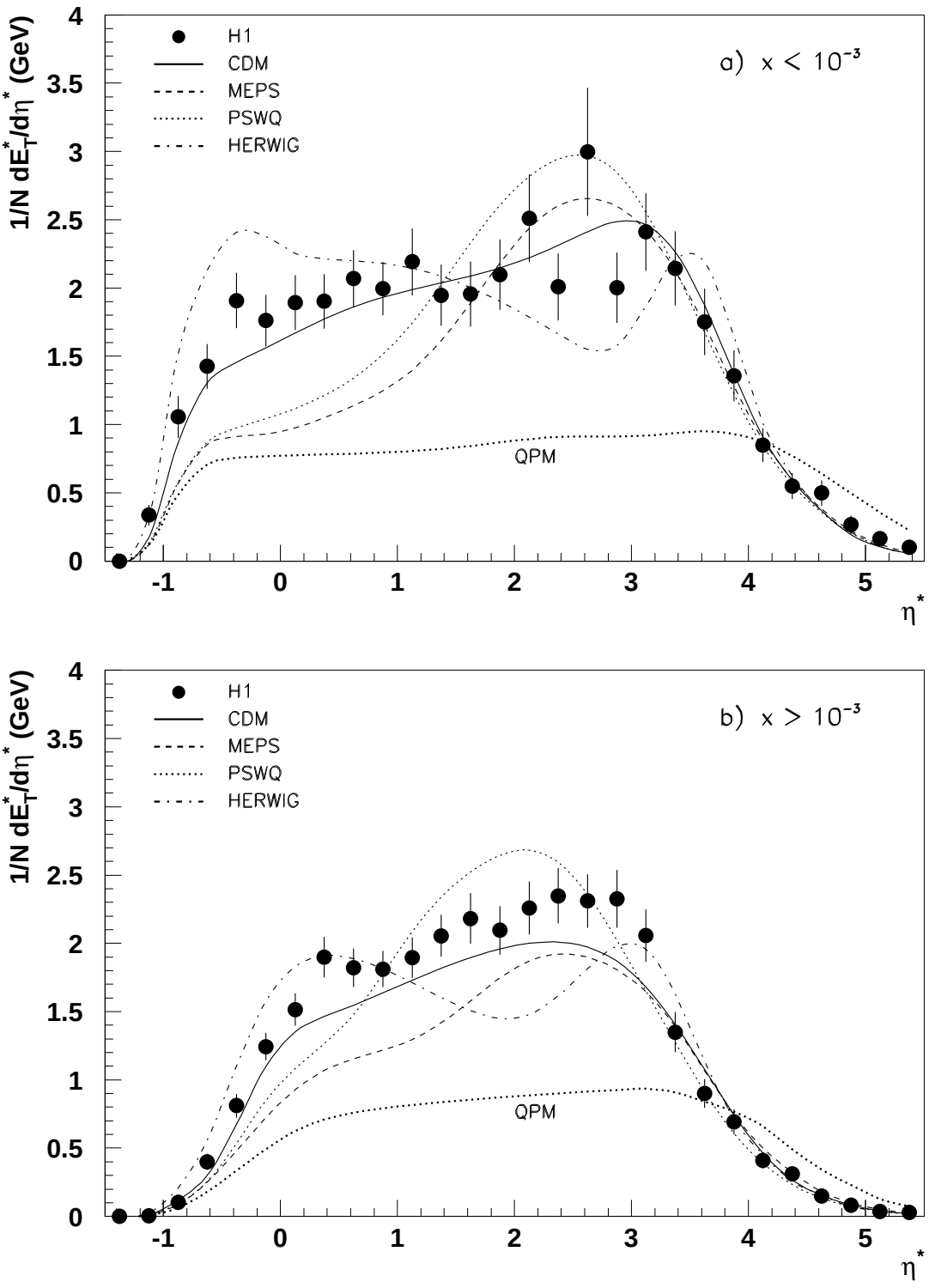

Figure 4: Transverse energy flows E_T^* in the hadronic center of mass system as a function of the pseudorapidity η^* for events with **a)** $x < 10^{-3}$ and **b)** $x > 10^{-3}$. The proton direction is to the left. The error bars contain the statistical and systematic errors added in quadrature, except for an overall 6% energy scale uncertainty.

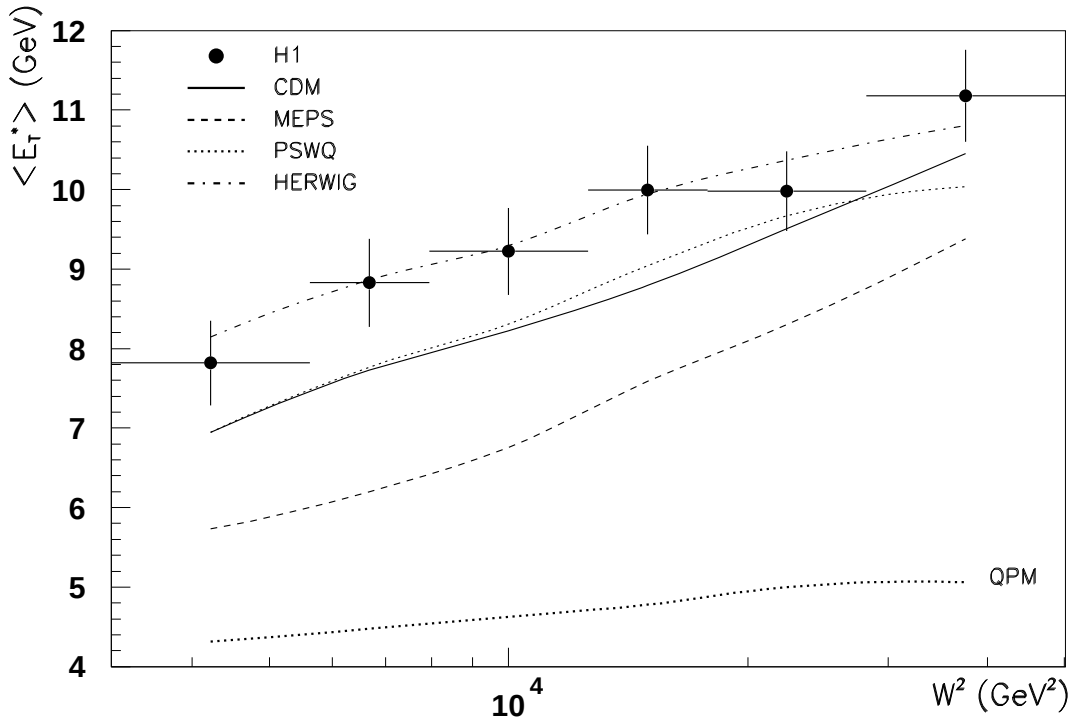

Figure 5: Mean transverse energy in the hadronic CMS as a function of W^2. The error bars contain the statistical and systematic errors added in quadrature, except for an overall 6% energy scale uncertainty.

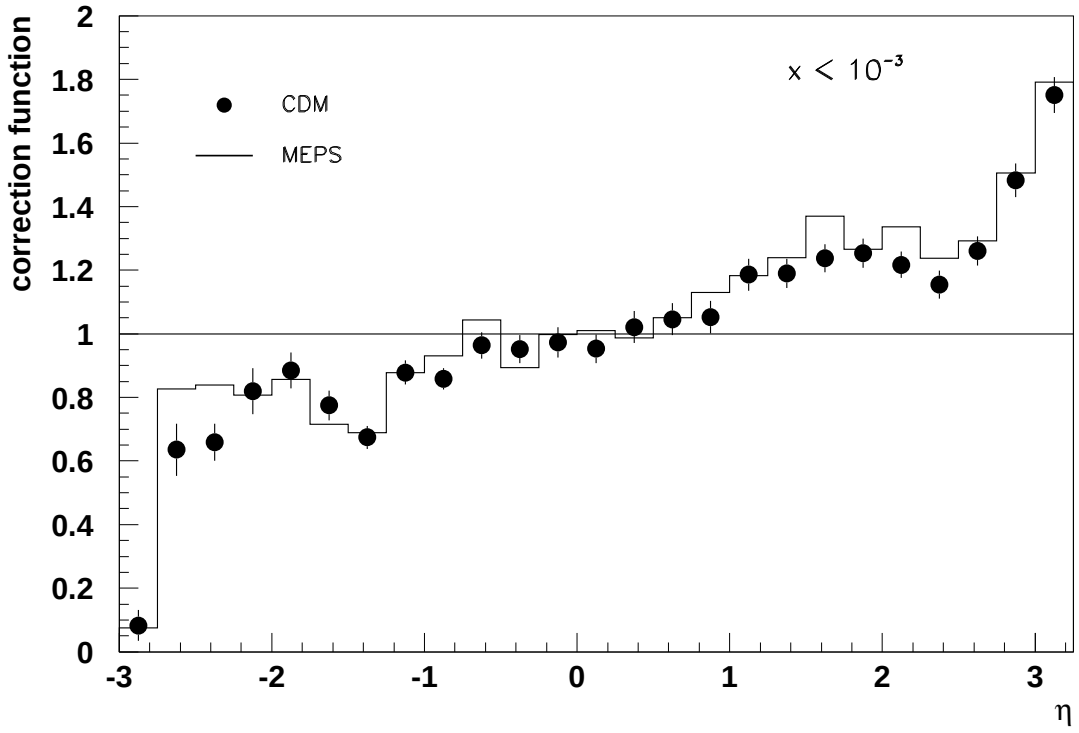

Figure 6: Correction function (reconstructed/generated values) for the transverse energy flow in the laboratory system for $x < 10^{-3}$. The proton direction is to the right.

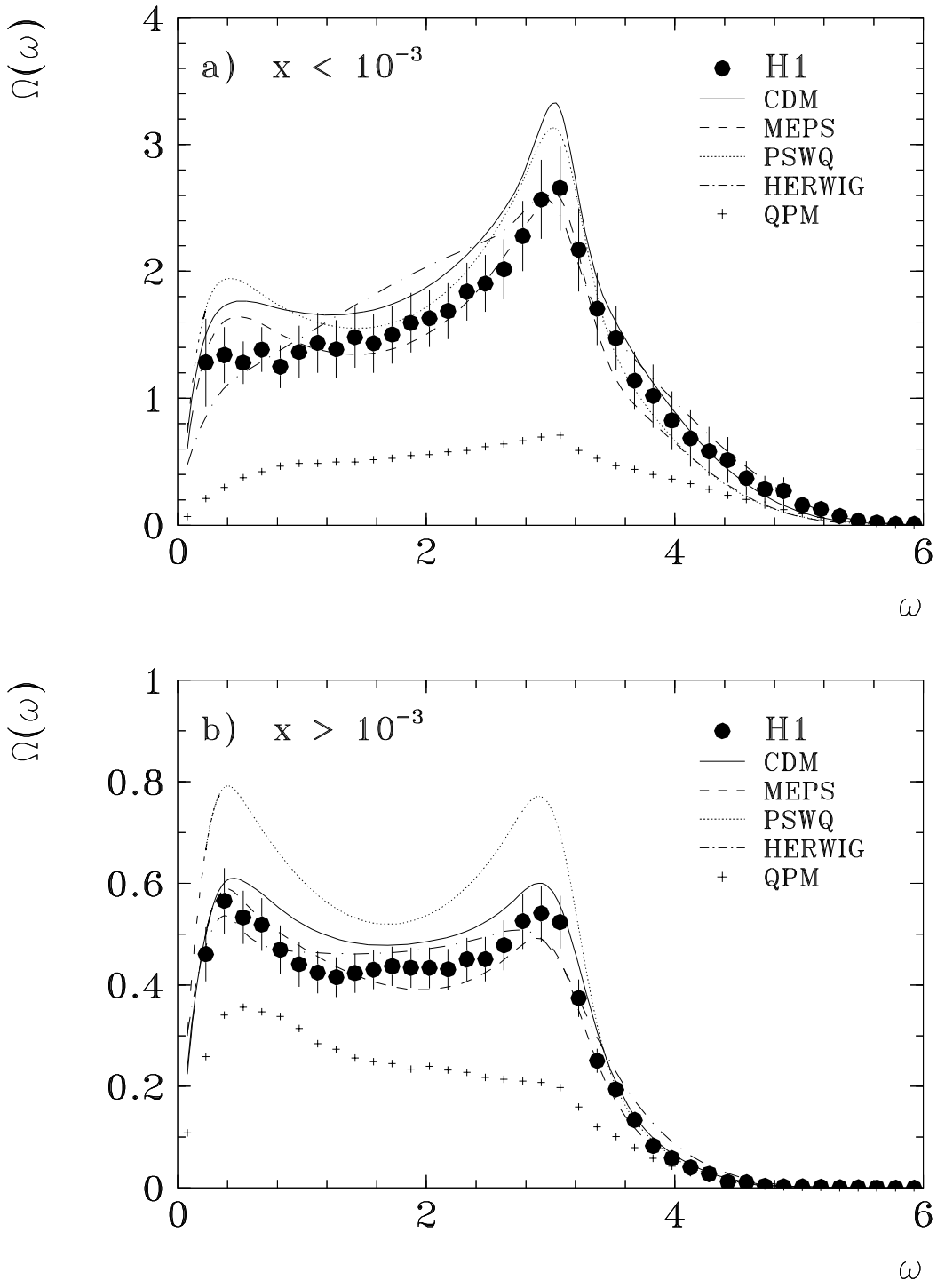

Figure 7: Transverse energy-energy correlations Ω in the laboratory system as a function of ω for events with **a)** $x < 10^{-3}$ and **b)** $x > 10^{-3}$. The error bars contain statistical and systematic errors added in quadrature; the overall systematic error of 12% from the energy scale is not included.

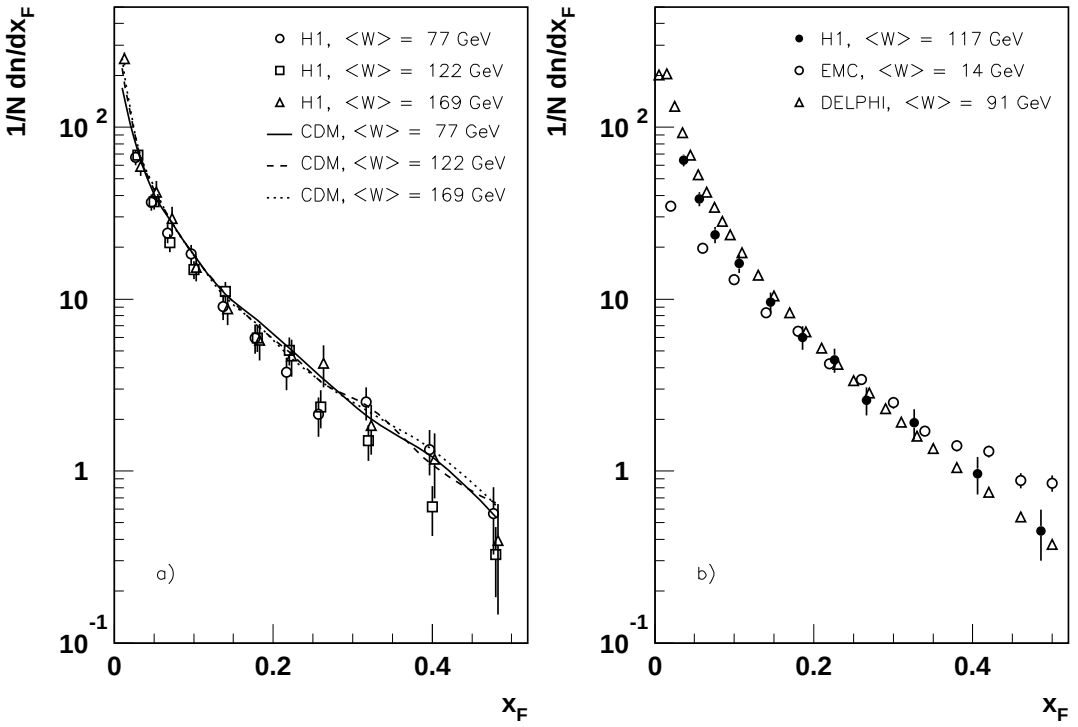

Figure 8: Scaled charged particle spectrum ($x_F = 2p_z^*/W$). The distributions are normalized to the number of events N, and n refers to the number of charged particles in a given bin. For the H1 data statistical and systematic errors are added in quadrature. In **a)** the H1 data for three different W bins are shown, together with the Monte Carlo which has been used for data correction (CDM). In **b)** the H1 data are compared with data from EMC and DELPHI. The DELPHI data are divided by two to account for the two jets in e^+e^-annihilation.

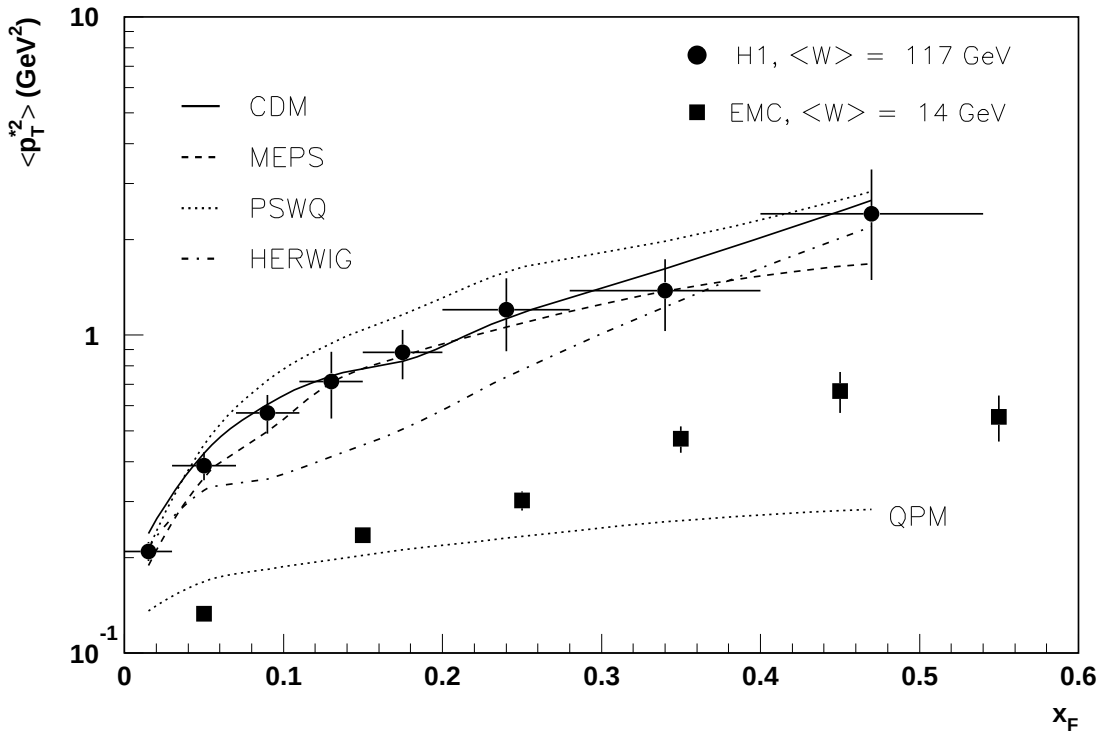

Figure 9: Seagull plot: average $p_T^{\star 2}$ as a function of $x_F = 2p_z^*/W$. The error bars for the H1 data contain statistical and systematic errors added in quadrature. Compared to the H1 data are the different model predictions and EMC data at lower W.